Nanoparticle Assembly Induced Ligand Interactions for Enhanced Electrocatalytic CO_2 Conversion

Sunmoon Yu,[1,3,†] Dohyung Kim,[1,2,3,†] Zhiyuan Qi,[4] Sheena Louisia,[2,3] Yifan Li,[2,3] Gabor A. Somorjai,[2,4] and Peidong Yang[1,2,3,5]*

[1]Department of Materials Science and Engineering, University of California, Berkeley, CA 94720, USA.

[2]Department of Chemistry, University of California, Berkeley, CA 94720, USA.

[3]Chemical Sciences Division, Lawrence Berkeley National Laboratory, Berkeley, CA 94720, USA.

[4]Materials Sciences Division, Lawrence Berkeley National Laboratory, Berkeley, CA 94720, USA.

[5]Kavli Energy NanoScience Institute, Berkeley, CA 94720, USA.

[†]These authors contributed equally to this work.

*Correspondence to: p_yang@berkeley.edu

ABSTRACT

The microenvironment in which the catalysts are situated is as important as the active sites in determining the overall catalytic performance. Recently, it has been found that nanoparticle (NP) surface ligands can actively participate in creating a favorable catalytic microenvironment, as part of the nanoparticle/ordered-ligand interlayer (NOLI), for selective CO_2 conversion. However, much of the ligand-ligand interactions presumed essential to the formation of such a catalytic interlayer remains to be understood. Here, by varying the initial size of NPs and utilizing spectroscopic and electrochemical techniques, we show that the assembly of NPs leads to the necessary ligand interactions for the NOLI formation. The large surface curvature of small NPs promotes strong non-covalent interactions between ligands of adjacent NPs through ligand interdigitation. This ensures their collective behavior in electrochemical conditions and gives rise to the structurally ordered ligand layer of the NOLI. Thus, the use of smaller NPs was shown to result in a greater catalytically effective NOLI area associated with desolvated cations and electrostatic stabilization of intermediates, leading to the enhancement of intrinsic CO_2-to-CO turnover. Our findings highlight the potential use of tailored microenvironments for NP catalysis by controlling its surface ligand interactions.

INTRODUCTION

Surface ligands are a crucial part of colloidal nanoparticles (NPs), controlling nucleation and growth during NP synthesis and allowing long-term stability of NPs in solution.[1] In addition, the organic surface ligands can significantly influence the surface properties of NPs affecting their use in many applications in areas such as catalysis and optoelectronics.[1-3] Hence, synthetic organic ligands of various structures and compositions have been studied to understand their influence and achieve the desired NP properties.[4-5] Furthermore, NP geometry (e.g., shape, size) can alter the ligand conformation and the intermolecular interaction between surface ligands.[6-7] In areas where precise control over ligand-to-ligand interaction is required, such as NP assembly, tuning the NP geometry has also been an effective method to control such interaction.[8]

In the field of electrochemical CO_2 conversion, NP surface ligands have recently gained great interest due to their potential benefits in facilitating the catalytic process. For example, they have been demonstrated as a molecular modifier electronically interacting with the NP surface and controlling the binding strength of the surface atomic sites.[9-10] Furthermore, certain ligands have been used to directly interact with CO_2 molecules or the relevant intermediates to enhance catalytic turnover and CO_2 reduction selectivity.[11-12] Moreover, ligand tail groups interfaced with the electrolyte may potentially alter mass transport affecting the availability of CO_2 and proton donors to the catalyst surface.[13-14]

Surface ligands can also be used to create a sophisticated catalytic microenvironment at the molecular level. Recently, we discovered an electrochemical interface so-called the nanoparticle/ordered-ligand interlayer (NOLI) that originates from the collective behavior of NP surface ligands.[15] The NOLI acts as a catalytic pocket by encompassing dehydrated cations and allowing intimate electrostatic interaction between the surface metal atom, dehydrated cation, and

CO_2 reduction intermediates (e.g., chemisorbed, bent CO_2, or b-$CO_2^{\delta-}$) that enhances catalytic activity by orders of magnitude (Figure 1). A unique feature of the NOLI is that the anionic surface ligands (e.g., alkylphosphonic acids) form a detached yet stable, structurally ordered ligand layer in the vicinity of the NP surface during CO_2 electrolysis. With an initial dense assembly of NPs found to be required, it was proposed that the strong interactions between the ligands at such a state allow the NOLI formation. However, it still remains uncertain as to how the initial NP assembly induces the needed strong ligand-ligand interactions and translates to the NOLI during CO_2 electrocatalysis. Detailed understanding of the structural requirements and operational mechanisms of complex nanostructures, such as the NOLI, is critical to improve upon their characteristics and find ways to create more advanced architectures.

Here, we investigate the effect of NP assembly on the surface ligand interactions and its resultant influence on the formation of the catalytic interlayer (i.e., NOLI). To this end, the initial condition of NP assembly is varied by employing monodisperse Ag NPs of different sizes. Spectroscopic evidence suggests that the large surface curvature of small NPs allows facile interdigitation of surface ligands during their assembly. The resulting strong intermolecular interaction promotes the formation of the NOLI, the extent of which governs the population of dehydrated cations associated. This unique catalytic microenvironment at the NP surface leads to a substantial intrinsic activity enhancement for CO_2-to-CO electroreduction.

This study unravels NP ligand interactions promoted by NP assembly and its intricate behavior during electrocatalysis. In addition, this work shows that geometric factors of NPs such as surface curvature may critically affect such ligand interactions. Overall, our findings suggest new opportunities for NP electrocatalyst design where NP ligand interactions are utilized to create

a favorable microenvironment for electrocatalytic reactions improving the intrinsic activity of catalysts.

RESULTS AND DISCUSSION

To alter the initial condition of NP assembly and thus the interactions between NP ligands, monodisperse Ag NPs with two different sizes (4 and 8 nm) were used (Figure S1). The NPs were colloidally synthesized using tetradecylphosphonic acid (TDPA) as surface ligands with both surfaces' having TDPA bound in a bidentate mode (Figure S2). They were drop-casted on a carbon paper support to achieve a densely packed NP assembly (Figure 2a, b).

With a negative potential sweep, both electrodes exhibited a cathodic peak attributed to the reductive dissociation of chemisorbed TDPA ligands as previously described (Figure S3a).[15] However, the reductive peak area of assembled 8 nm Ag NPs (2.00 mC) was relatively smaller than that of assembled 4 nm Ag NPs (3.21 mC). It should be noted that the absolute amount of ligands on each electrode were identical (by controlling the total NP loading, see Methods) and the theoretical charge estimate for complete ligand dissociation is 3.25 mC. Thus, some fraction of ligands remains chemisorbed for the 8 nm Ag NPs under bias. In contrast, 4 nm Ag NPs exhibit collective dissociation of chemisorbed ligands to the full extent.

Both electrodes showed reversible physisorption features of the ligands in the following cyclic voltammetry (CV) scans, indicating the ordered-ligand layer formed by collective dissociation (Figure S3b). While the presence of such suggests the formation of NOLI for both,[15] the charge area covered by reversible physisorption of the 8 nm Ag NPs was smaller than that of the 4 nm Ag NPs, hinting at limited collective dissociation of surface ligands for the 8 nm Ag NPs

as expected. Therefore, the voltammetry results suggest only partial transformation of the surface ligands to the ordered-ligand layer as part of the NOLI for the 8 nm Ag NPs.

In addition, the initial dissociation of chemisorbed ligands from the NP surface allowed NP growth through interparticle fusion (Figure 1), a characteristic feature of the NOLI.[15] Figure 2c and d show the Ag-NOLI catalysts derived from the assembled 4 nm and 8 nm Ag NPs at –0.68 V vs. RHE in 0.1 M $KHCO_3$, respectively. The resultant Ag-NOLI catalysts are referred to as X-Ag-NOLI throughout this work where X is the initial size of the pristine NP.

Both Ag-NOLI catalysts showed notably improved catalytic reactivity as shown in their high current density compared to polycrystalline Ag foil under CO_2-reducing conditions (Figure S4a, b). In addition, they exhibited high selectivity towards CO compared to Ag foil reaching >94% (Figure 3a, Table S1). Also, to compare the intrinsic activity of catalysts, Pb underpotential deposition method was used to measure the electrochemically active surface area (Figure S4c). The Ag-NOLI catalysts exhibited >10-fold improved specific CO current densities compared to Ag foil at –0.68 V (Figure 3b). However, when the ligand layer and thus the NOLI were removed from both catalysts (4-Ag-NOLI and 8-Ag-NOLI), comparable specific CO current densities to that of Ag foil were recorded (Figure 3b, S5). This confirms that the unique configuration of the Ag-NOLI catalysts, that is, the NOLI, enhances their intrinsic activity, as previously reported.[15]

When Ag NPs were initially isolated from each other, both particles exhibited poor CO selectivity as previously reported (<40%, Figure S6).[15] Absence of the collective ligand dissociation and characteristic ligand adsorption/desorption confirm that the NOLI does not form starting from such configuration (Figure S6).[15] Thus, we find that, regardless of initial NP size, NP assembly and the associated ligand interactions are necessary for NOLI formation.

Interestingly, 4-Ag-NOLI also showed a more than two-fold enhancement in specific CO activity compared to 8-Ag-NOLI, while its specific current density towards H_2 remained comparable (Figure 3c, d). The average sizes of 4-Ag-NOLI and 8-Ag-NOLI catalysts (30.2 and 39.8 nm, respectively, Figure 2c, d) are both in a regime whose size dependent activity enhancement is known to be negligible.[16] Also, their crystallite size were similar (23.3 and 25.8 nm) after CO_2 electrolysis (Figure S7) ruling out any enhancement by such. Therefore, in agreement with our previous report, the morphological factors of Ag particles do not seem critical to the activity of Ag-NOLI catalysts.[15] Instead, the structural details of the NOLI may not be equivalent between the two as may be suspected from the partial transformation of the surface ligand to the ordered-ligand layer exhibited by the 8 nm NPs (Figure S3).

Considering the importance of NP assembly and how it affects the ligand behavior under bias, the initial configuration of ligands on isolated and assembled Ag NPs were studied by sum frequency generation (SFG) vibrational spectroscopy. As a second-order nonlinear spectroscopic technique, SFG is particularly surface sensitive and thus suited for studying NP surface ligands (e.g., molecular conformation, structural order).[17-19] For the ligand alkyl chain, all-trans conformation results in negligibly weak intensities for methylene (CH_2) stretch modes (d^+, d^-, symmetric and asymmetric stretch, respectively) due to its approximate inversion symmetry. Instead, SFG intensities for methyl (CH_3) stretch modes (r^+, r^-) dominate, as observed in TDPA crystals and self-assembled monolayers of TDPA on a flat Ag film (Figure S8). However, when gauche defects along the alkyl chain are present as part of ligand disorder, the inversion symmetry is broken, allowing signals at the methylene stretch modes. Therefore, the SFG intensity ratio between d^+ and r^+ (or d^- and r^-) can be used to gauge the structural order of ligands on NP surfaces.[18, 20]

SFG spectra of TDPA-capped Ag NPs in the CH-stretch region (2800-3000 cm^{-1}) exhibited four C–H stretch bands: methylene symmetric stretch (d^+), methylene asymmetric stretch (d^-), methyl symmetric stretch (r^+), and methyl asymmetric out-of-plane stretch (r^-_{op}) (Figure 4a, b). The appearance of the methylene stretch bands in the SFG spectra indicates the presence of gauche defects.[18] For the isolated NPs, the intensity ratio of d^+ to r^+ for the 4 nm Ag NPs was higher than that of 8 nm Ag NPs (Figure 4a-c), suggesting more gauche defects present. This size-dependent trend is due to the three-dimensional volume for each ligand made available by the NP surface curvature allowing the ligand chains to entropically explore and induce gauche defects.[18] In the case of the TDPA-coated flat Ag film, whose surface curvature is close to zero, gauche defects were negligible (Figure S8). Therefore, ligands on smaller NPs with a larger surface curvature tend to have more gauche defects than those on larger ones with a smaller surface curvature.

Interestingly, when 4 nm Ag NPs are assembled, the d^+ intensity substantially decreases relative to r^+. This suggests a transition from disordered to ordered ligand configuration (Figure 4a, c). On the other hand, there is only a slight decrease in the d^+/r^+ ratio for the 8 nm Ag NPs (Figure 4b, c). This difference pertains to the free volume available for ligand interdigitation during NP assembly. As illustrated in Figure 4d, the 4 nm NPs have a larger cylindrical volume per ligand owing to their lower ligand packing density at the exterior away from the surface. The ligand packing density of 4 nm and 8 nm NPs are 0.25 and 0.44 at the end of the ligand tail, respectively (Figure S9).[18, 21] This permits facile interdigitation of ligands from adjacent 4 nm NPs when assembled, promoting intimate ligand-ligand interactions and structural inter-chain ordering.[22] The resultant ligand network, molecularly linking NPs, can collectively dissociate from NP surfaces under bias (Figure S3a).

In contrast, ligands on isolated 8 nm NPs with a smaller surface curvature are already well-ordered as less volume is available for each ligand (Figure 4c, Table S2). However, this close packing of the ligands is not conducive to ligand interdigitation from neighboring NPs, as illustrated in Figure 4d. As a result, the assembly of 8 nm NPs exhibit only a negligible change in the d^+/r^+ ratio (Figure 4c). The resulting weak interaction between the ligands of adjacent NPs seems to be the cause of their limited collective behavior as observed from their partial reductive dissociation (Figure S3a). The ligand-ligand interaction between neighboring NPs can also be indirectly probed by measuring interparticle distance. The smaller gap measured between the assembled 4 nm NPs compared to that of the assembled 8 nm NPs implies a greater extent of ligand interdigitation and enhanced non-covalent interaction between ligand chains (Figure S10).

The transition of interdigitated surface ligands to an ordered-ligand layer under bias was studied by X-ray photoelectron spectroscopy (XPS) (Figure 5a, b). For the assembled 4 nm Ag NPs, the peak shift in P 2*p* and complete loss of the P-O-Ag peak in O 1*s* indicate that the TDPA ligands initially chemisorbed completely transitioned to a physisorbed state after negative bias (–0.68 V vs. RHE) was applied (Figure 5a). In contrast, for the assembled 8 nm Ag NPs, as foreseen from the partial ligand dissociation upon reductive potential sweep, the P 2*p* and O 1*s* spectra revealed that some fraction of ligands remains chemisorbed (Figure 5b).

For comparison, the deconvoluted P 2*p* peaks representing chemisorbed and physisorbed ligands were integrated (identical XPS measurement parameters were used for quantitative analysis, see Methods for details) (Figure 5c). The absolute amount of ligands that are dissociated upon bias and participate in the formation of an ordered-ligand layer was much smaller for 8-Ag-NOLI with only 63% of all ligands being in such a state.

The overall process of the ordered-ligand layer formation is described in Figure 5d, e. For the assembled 4 nm Ag NPs, ligands between neighboring NPs can be readily interdigitated, promoting ligand-ligand interactions. This allows collective dissociation of all ligands under bias. On the other hand, for the assembled 8 nm NPs, limited ligand interdigitation results in the partial transformation to an ordered-ligand layer with some ligands remaining chemisorbed. As a result, physisorbed and chemisorbed ligand states co-exist in 8-Ag-NOLI. Furthermore, for TDPA-coated flat Ag substrate where there is no ligand interdigitation, it was previously shown that ligands display a lack of collective behavior, that is, inidivual ligand loss under bias and absence of reversible physisorption as well as exisitence of mixed physisorbed and chemisorbed ligand states.[15] These results reinforce that the ligand interdigitation by NP assembly and resulting strong intermolecular interactions are a precondition to the NOLI formation.

Importantly, the ligand density on the catalyst surface is crucial, as it relates to the extent of the unique microenvironment afforded by the NOLI per Ag area basis. One important consideration for this comparison is the NP fusion and reduction in surface area that coincides with NOLI formation. Thus, the morphological changes of both Ag NPs were tracked during CO_2 electroreduction (Figure S11, 12). The 4 nm Ag NPs exhibited a more rapid NP growth at −0.68 V compared to the 8 nm NPs (Figure S13). We attribute this difference to the extent of collective dissociation of interdigitated ligands that expose the surfaces of neighboring NPs (Figure 5c). Using XPS, we probed the P at.% (with P at.% + Ag at.% = 100%) during CO_2 electrolysis, which showed consistently much higher physisorbed P at.% for 4-Ag-NOLI (Figure S14, 15). Taken together, 4-Ag-NOLI is expected to have a higher ligand layer density, or equivalently, a larger effective NOLI area per Ag surface area.

In addition, after the formation of an ordered-ligand layer, the absolute amount of physisorbed ligands for 4-Ag-NOLI during one-hour electrolysis was much larger than that of 8-Ag-NOLI (Figure S16). The improved retention of the ligand layer in 4-Ag-NOLI and its structural order (Figure S17) should result from their stronger ligand-ligand interactions enabled by the facile ligand interdigitation.

The structure of the ligand layer formed and its surface coverage can be deduced by combining the spectroscopic results (SFG and XPS) (Figure 6). The initial surface coverage on pristine Ag NPs can be estimated from the XPS results (Figure S18). Pristine 4 and 8 nm Ag NPs were found to have a complete monolayer ligand coverage (~100%).[15] Meanwhile, the surface coverage of the ligand layer formed on the Ag-NOLI catalysts during CO_2 electrocatalysis can be estimated assuming two boundary model structures: (i) a monolayer structure and (ii) a bilayer structure (Figure S18).

For 4-Ag-NOLI, when the monolayer configuration is assumed, the ligand layer coverage exceeds the theoretical complete coverage. Considering the interdigitation of ligands in the 4 nm Ag NP assembly, this implies that the ligand layer may likely possess a bilayer structure.[23] When the bilayer ligand configuration is assumed, the ligand layer coverage is close to 100% (Figure 6a). This suggests that the initial interdigitated ligand network with strong intermolecular forces is key to the formation of the ordered-ligand layer near the catalyst surface under bias (Figure 6c). The decrease in the ligand layer coverage with the bilayer configuration assumed after 20 min may be due to partial ligand loss from the outer layer of the bilayer structure (Figure 6a, c).[23]

On the other hand, for 8-Ag-NOLI, there is some fraction of the ligands that remain chemisorbed throughout one-hour CO_2 electrolysis (Figure 6b and S14). The physisorbed layer crucial to the NOLI only occupies part of the Ag surface, in contrast to 4-Ag-NOLI (Figure 6b, d,

and S18). Therefore, we find that 4-Ag-NOLI possesses a larger effective NOLI area for facilitating CO_2-to-CO electroreduction.

During CO_2 electrolysis, both 4-Ag-NOLI and 8-Ag-NOLI exhibited pseudocapacitive features in the CV scans (Figure S19) characteristic of the NOLI.[15] Electrochemical impedance spectroscopy (EIS) also shows that both Ag-NOLI catalysts exhibit a small semi-circle in the high frequency region of the Nyquist plot (Figure 7a and S20). As previously described, this feature results from the pseudocapacitive behavior of the NOLI.[15] The EIS data were fitted using an equivalent circuit including a pseudocapacitance element. Both exhibited notably high specific capacitance values compared to typical metal electrodes (for instance, polycrystalline Ag foil previously showed 34.6 $\mu F/cm^2$ in the same electrochemical condition) (Figure 7b).[15, 24] Also, when the NOLI was removed from the Ag-NOLI catalysts, the pseudocapacitive features were lost (Figure S21).

Furthermore, 4-Ag-NOLI showed about a two-fold higher specific capacitance value compared to 8-Ag-NOLI (Figure 7b and Table S3). The pseudocapacitive charge is specifically associated with the amount of desolvated cations interposed at the interlayer. Therefore, the relatively high specific capacitance of 4-Ag-NOLI offers further support for the larger effective NOLI area over the Ag surface, as predicted from spectroscopy.

Recently, to harness the interplay between CO_2 molecules and electrolyte species, the catalytic effect of electrolyte cations has been investigated.[25-27] Several studies have proposed that cations can electrostatically stabilize CO_2 at the electrochemical interface, serving as a promoter.[27-28] In our previous study, we have demonstrated that desolvated cations at the NOLI facilitate the first electron transfer ($CO_2 + e^- \rightarrow CO_2^{\bullet-}$) by stabilizing adsorbed CO_2 molecules (b-$CO_2^{\delta-}$).[15] The desolvated cations unique to the NOLI were found to achieve this more effectively through

enhanced electrostatic interactions.[15] Hence, the extended effective NOLI area between the catalyst surface and the structurally ordered ligand layer (Figure S17) available for 4-Ag-NOLI is what leads to its significantly improved intrinsic activity (i.e., specific current density towards CO) (Figure 3c).

In light of the importance of intermolecular interactions between ligand chains for both the formation and sustenance of a catalytically favorable microenvironment (Figure S22), we envision that NOLI can be constructed and improved by the modular selection of its components. For example, ligands with intrinsically stronger interactions (van der Waals, electrostatic, and even hydrogen bonding) can be employed.[8] Besides, the geometry of the NP core such as its surface curvature and shape needs to be carefully considered for the NP assembly-induced ligand interactions. For instance, small NPs below 4 nm (ref.[29]) can be utilized for enhanced NP assembly-induced ligand interactions. Furthermore, functional groups that can interact with CO_2 molecules (e.g., an imidazole group) may be included in the ligand chain to regulate local CO_2 transport.[13] Lastly, molecular catalysts may be coupled with the NOLI catalysts for tandem CO_2 electrolysis by having a catalytically active moiety in the ligand chain[30] and potentially expanding the applicability of the NOLI catalysts for various reactions.

CONCLUSIONS

In this study, we show that NP assembly promotes non-covalent interactions between NP surface ligands via ligand interdigitation, which is vital for the formation of a structurally ordered-ligand layer over the catalyst surface during CO_2 electrocatalysis. The large surface curvature of NPs plays an important role in facilitating the ligand interdigitation and intimate intermolecular interaction between its chains. Through strong ligand-ligand interactions, a unique

microenvironment at the electrochemical interface (the nanoparticle/ordered-ligand interlayer, or NOLI) is created under bias, improving catalytic activity and selectivity for CO_2-to-CO electroconversion. Furthermore, the catalytically effective area of NOLI is found to be dependent on the extent of the ligand interactions induced by NP assembly. Based on this understanding, we expect that NP catalysts with tailored microenvironments can be developed by harnessing the NP assembly-induced ligand interactions and employing specific ligands with added functionality to control activity and selectivity for various electrocatalytic reactions.

ASSOCIATED CONTENT

Supporting Information

Experimental methods, additional characterization data including SEM and TEM images, SFG and XPS spectra, XRD patterns, and electrochemical data (PDF)

AUTHOR INFORMATION

Corresponding Author

*p_yang@berkeley.edu

Author Contributions

†S.Y. and D.K. contributed equally.

Notes

The authors declare no competing financial interest.

ACKNOWLEDGEMENT

This work was supported by the Director, Office of Science, Office of Basic Energy Sciences, Chemical Sciences, Geosciences, & Biosciences Division, of the U.S. Department of Energy under contract no. DE-AC02-05CH11231, FWP CH030201 (Catalysis Research Program). Work at the Molecular Foundry was supported by the Director, Office of Science, Office of Basic Energy Sciences, of the U.S. Department of Energy under contract no. DE-AC02-05CH11231. ICP-OES was supported by the Microanalytical Facility, College of Chemistry, University of California, Berkeley. S.Y. and D.K. acknowledge support from Samsung Scholarship.

REFERENCES

1. Boles, M. A.; Ling, D.; Hyeon, T.; Talapin, D. V., The surface science of nanocrystals. *Nat. Mater.* **2016**, *15* (2), 141-153.
2. Lu, L.; Zou, S.; Fang, B., The Critical Impacts of Ligands on Heterogeneous Nanocatalysis: A Review. *ACS Catal.* **2021**, *11* (10), 6020-6058.
3. Brown, P. R.; Kim, D.; Lunt, R. R.; Zhao, N.; Bawendi, M. G.; Grossman, J. C.; Bulovic, V., Energy Level Modification in Lead Sulfide Quantum Dot Thin Films through Ligand Exchange. *ACS Nano* **2014**, *8* (6), 5863-5872.
4. De Roo, J.; Zhou, Z.; Wang, J.; Deblock, L.; Crosby, A. J.; Owen, J. S.; Nonnenmann, S. S., Synthesis of Phosphonic Acid Ligands for Nanocrystal Surface Functionalization and Solution Processed Memristors. *Chem. Mater.* **2018**, *30* (21), 8034-8039.
5. Westmoreland, D. E.; López-Arteaga, R.; Weiss, E. A., N-Heterocyclic Carbenes as Reversible Exciton-Delocalizing Ligands for Photoluminescent Quantum Dots. *J. Am. Chem. Soc.* **2020**, *142* (5), 2690-2696.
6. Walker, D. A.; Leitsch, E. K.; Nap, R. J.; Szleifer, I.; Grzybowski, B. A., Geometric curvature controls the chemical patchiness and self-assembly of nanoparticles. *Nat. Nanotechnol.* **2013**, *8* (9), 676-681.
7. Wu, M.; Vartanian, A. M.; Chong, G.; Pandiakumar, A. K.; Hamers, R. J.; Hernandez, R.; Murphy, C. J., Solution NMR Analysis of Ligand Environment in Quaternary Ammonium-Terminated Self-Assembled Monolayers on Gold Nanoparticles: The Effect of Surface Curvature and Ligand Structure. *J. Am. Chem. Soc.* **2019**, *141* (10), 4316-4327.
8. Si, K. J.; Chen, Y.; Shi, Q.; Cheng, W., Nanoparticle Superlattices: The Roles of Soft Ligands. *Adv. Sci.* **2018**, *5* (1), 1700179.
9. Kim, C.; Jeon, H. S.; Eom, T.; Jee, M. S.; Kim, H.; Friend, C. M.; Min, B. K.; Hwang, Y. J., Achieving Selective and Efficient Electrocatalytic Activity for CO_2 Reduction Using Immobilized Silver Nanoparticles. *J. Am. Chem. Soc.* **2015**, *137* (43), 13844-13850.
10. Zhao, Y.; Wang, C. Y.; Liu, Y. Q.; MacFarlane, D. R.; Wallace, G. G., Engineering Surface Amine Modifiers of Ultrasmall Gold Nanoparticles Supported on Reduced Graphene Oxide for Improved Electrochemical CO_2 Reduction. *Adv. Energy Mater.* **2018**, *8* (25), 1801400.
11. Wang, Z.; Wu, L.; Sun, K.; Chen, T.; Jiang, Z.; Cheng, T.; Goddard, W. A., 3rd, Surface Ligand Promotion of Carbon Dioxide Reduction through Stabilizing Chemisorbed Reactive Intermediates. *J. Phys. Chem. Lett.* **2018**, *9* (11), 3057-3061.
12. Cao, Z.; Zacate, S. B.; Sun, X.; Liu, J.; Hale, E. M.; Carson, W. P.; Tyndall, S. B.; Xu, J.; Liu, X.; Liu, X.; Song, C.; Luo, J. H.; Cheng, M. J.; Wen, X.; Liu, W., Tuning Gold Nanoparticles with Chelating Ligands for Highly Efficient Electrocatalytic CO_2 Reduction. *Angew. Chem. Int. Ed.* **2018**, *57* (39), 12675-12679.
13. Pankhurst, J. R.; Guntern, Y. T.; Mensi, M.; Buonsanti, R., Molecular tunability of surface-functionalized metal nanocrystals for selective electrochemical CO_2 reduction. *Chem. Sci.* **2019**, *10* (44), 10356-10365.
14. Wakerley, D.; Lamaison, S.; Ozanam, F.; Menguy, N.; Mercier, D.; Marcus, P.; Fontecave, M.; Mougel, V., Bio-inspired hydrophobicity promotes CO_2 reduction on a Cu surface. *Nat. Mater.* **2019**, *18* (11), 1222-1227.

15. Kim, D.; Yu, S.; Zheng, F.; Roh, I.; Li, Y.; Louisia, S.; Qi, Z.; Somorjai, G. A.; Frei, H.; Wang, L.-W.; Yang, P., Selective CO_2 electrocatalysis at the pseudocapacitive nanoparticle/ordered-ligand interlayer. *Nat. Energy* **2020**, *5* (12), 1032-1042.
16. Zhu, W.; Michalsky, R.; Metin, O.; Lv, H.; Guo, S.; Wright, C. J.; Sun, X.; Peterson, A. A.; Sun, S., Monodisperse Au nanoparticles for selective electrocatalytic reduction of CO_2 to CO. *J. Am. Chem. Soc.* **2013**, *135* (45), 16833-16836.
17. Humbert, C.; Noblet, T.; Dalstein, L.; Busson, B.; Barbillon, G., Sum-Frequency Generation Spectroscopy of Plasmonic Nanomaterials: A Review. *Materials* **2019**, *12* (5), 836.
18. Weeraman, C.; Yatawara, A. K.; Bordenyuk, A. N.; Benderskii, A. V., Effect of nanoscale geometry on molecular conformation: vibrational sum-frequency generation of alkanethiols on gold nanoparticles. *J. Am. Chem. Soc.* **2006**, *128* (44), 14244-14245.
19. Jacob, J. D. C.; Lee, T. R.; Baldelli, S., In Situ Vibrational Study of the Reductive Desorption of Alkanethiol Monolayers on Gold by Sum Frequency Generation Spectroscopy. *J. Phys. Chem. C* **2014**, *118* (50), 29126-29134.
20. Xiao, Q.; Xi, Y.; Wang, J.; Tu, D.; You, W.; Ye, X.; Liu, H.; Chen, X.; Lin, H., Combined In Situ Spectroscopies Reveal the Ligand Ordering-Modulated Photoluminescence of Upconverting Nanoparticles. *J. Phys. Chem. C* **2020**, *124* (42), 23086-23093.
21. Heinz, H.; Vaia, R. A.; Farmer, B. L., Relation between packing density and thermal transitions of alkyl chains on layered silicate and metal surfaces. *Langmuir* **2008**, *24* (8), 3727-3733.
22. O'Donnell, A.; Yach, K.; Reven, L., Particle-particle interactions and chain dynamics of fluorocarbon and hydrocarbon functionalized ZrO_2 nanoparticles. *Langmuir* **2008**, *24* (6), 2465-2471.
23. Nikoobakht, B.; El-Sayed, M. A., Evidence for bilayer assembly of cationic surfactants on the surface of gold nanorods. *Langmuir* **2001**, *17* (20), 6368-6374.
24. Strmcnik, D.; van der Vliet, D. F.; Chang, K. C.; Komanicky, V.; Kodama, K.; You, H.; Stamenkovic, V. R.; Markovic, N. M., Effects of Li^+, K^+, and Ba^{2+} Cations on the ORR at Model and High Surface Area Pt and Au Surfaces in Alkaline Solutions. *J. Phys. Chem. Lett.* **2011**, *2* (21), 2733-2736.
25. Moura de Salles Pupo, M.; Kortlever, R., Electrolyte Effects on the Electrochemical Reduction of CO_2. *ChemPhysChem* **2019**, *20* (22), 2926-2935.
26. Aran-Ais, R. M.; Gao, D.; Roldan Cuenya, B., Structure- and Electrolyte-Sensitivity in CO_2 Electroreduction. *Acc. Chem. Res.* **2018**, *51* (11), 2906-2917.
27. Ringe, S.; Clark, E. L.; Resasco, J.; Walton, A.; Seger, B.; Bell, A. T.; Chan, K., Understanding cation effects in electrochemical CO_2 reduction. *Energy Environ. Sci.* **2019**, *12* (10), 3001-3014.
28. Chen, L. D.; Urushihara, M.; Chan, K. R.; Norskov, J. K., Electric Field Effects in Electrochemical CO_2 Reduction. *ACS Catal.* **2016**, *6* (10), 7133-7139.
29. Li, P.; Peng, Q.; Li, Y., Controlled Synthesis and Self-Assembly of Highly Monodisperse Ag and Ag_2S Nanocrystals. *Chem. Eur. J.* **2011**, 17 (3), 941-946.
30. Li, F.; Li, Y. C.; Wang, Z.; Li, J.; Nam, D.-H.; Lum, Y.; Luo, M.; Wang, X.; Ozden, A.; Hung, S.-F.; Chen, B.; Wang, Y.; Wicks, J.; Xu, Y.; Li, Y.; Gabardo, C. M.; Dinh, C.-T.; Wang, Y.; Zhuang, T.-T.; Sinton, D.; Sargent, E. H., Cooperative CO_2-to-ethanol conversion via enriched intermediates at molecule–metal catalyst interfaces. *Nat. Catal.* **2019**, *3* (1), 75-82.

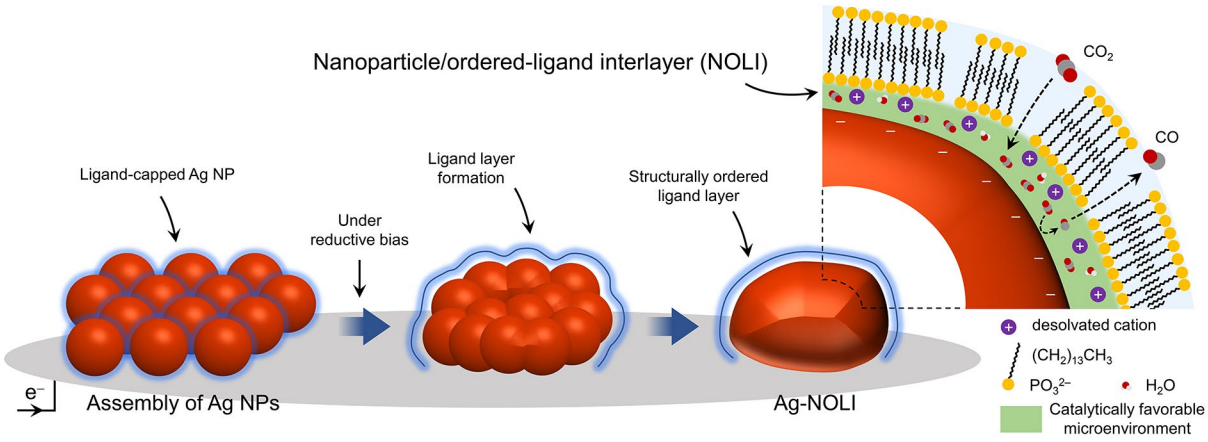

Figure 1. Schematic illustration of NOLI formation and its effect in CO_2 electrocatalysis. Surface ligands (tetradecylphosphonic acid) are initially covalently bonded to the nanoparticle (NP) surface. Upon biasing under CO_2-reducing conditions (0.1 M $KHCO_3$ saturated with 1 atm CO_2), the ligands collectively detach and form a structurally ordered ligand layer. The starting small NPs also fuse into a larger NP during the process. The initial interaction between ligands induced by NP assembly is considered crucial for the NOLI formation.

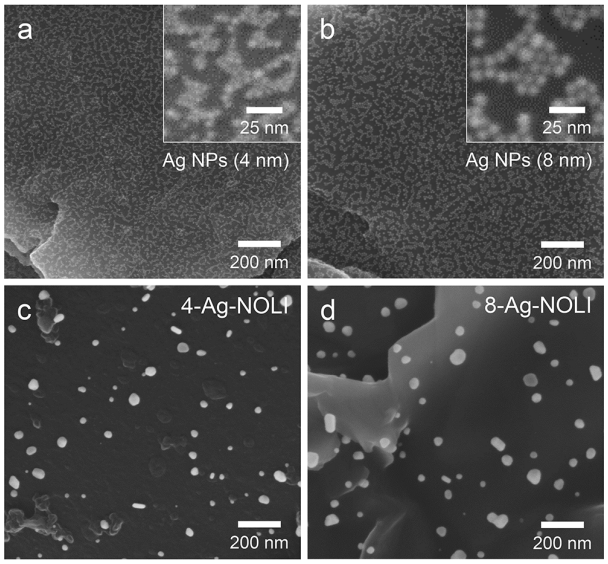

Figure 2. Initial Ag nanoparticle assembly for Ag-NOLI catalyst formation. a, **b**, Scanning electron microscopy (SEM) images of assembled 4 nm (**a**) and 8 nm (**b**) Ag NPs. **c**, **d**, SEM images of 4-Ag-NOLI (**c**) and 8-Ag-NOLI (**d**) catalysts derived from assembled 4 and 8 nm Ag NPs, respectively, under bias in a CO_2-reducing condition (–0.68 V vs. RHE for 60 min).

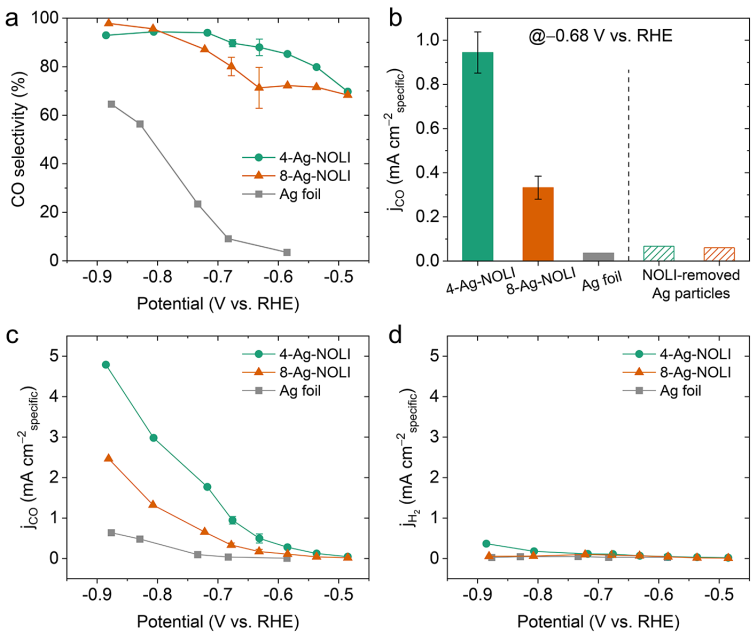

Figure 3. Electrocatalytic performance comparison. a, CO selectivity comparison between 4-Ag-NOLI, 8-Ag-NOLI, and Ag foil at various applied potentials. **b**, Specific CO current density comparison between Ag-NOLI catalysts, Ag foil, and NOLI-removed Ag particles at –0.68 V vs. RHE (hatched green and brown columns represent 4-Ag-NOLI and 8-Ag-NOLI after the NOLI removal, respectively). **c**, **d**, Specific current density of 4-Ag-NOLI, 8-Ag-NOLI, and Ag foil towards CO (**c**) and H_2 (**d**) at a range of applied potentials.

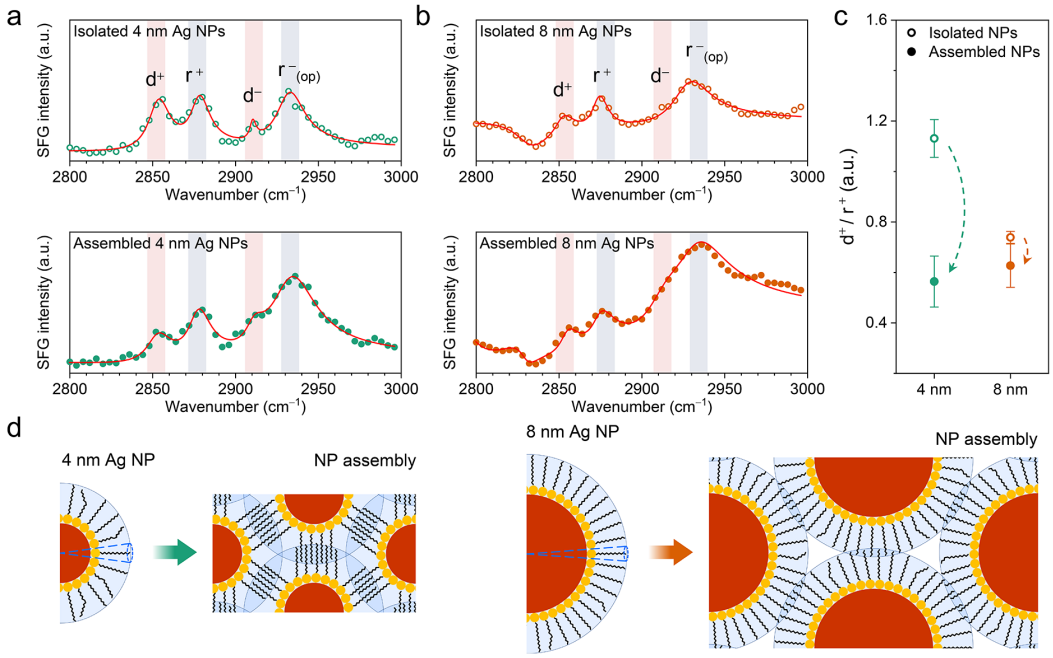

Figure 4. Nanoparticle assembly induced ligand interdigitation. **a**, **b**, Sum frequency generation (SFG) spectra of isolated (top) and assembled (bottom) 4 nm (**a**) and 8 nm (**b**) Ag NPs. Red curves are fitted lines (see Methods for details about fitting). **c**, SFG peak amplitude ratio of methylene symmetric stretch (d^+) to methyl symmetric stretch (r^+) before and after assembly of 4 and 8 nm Ag NPs. **d**, Schematics illustrating the impact of nanoparticle surface curvature on ligand interdigitation. Blue dashed lines indicate cylindrical space available for individual ligands before NP assembly.

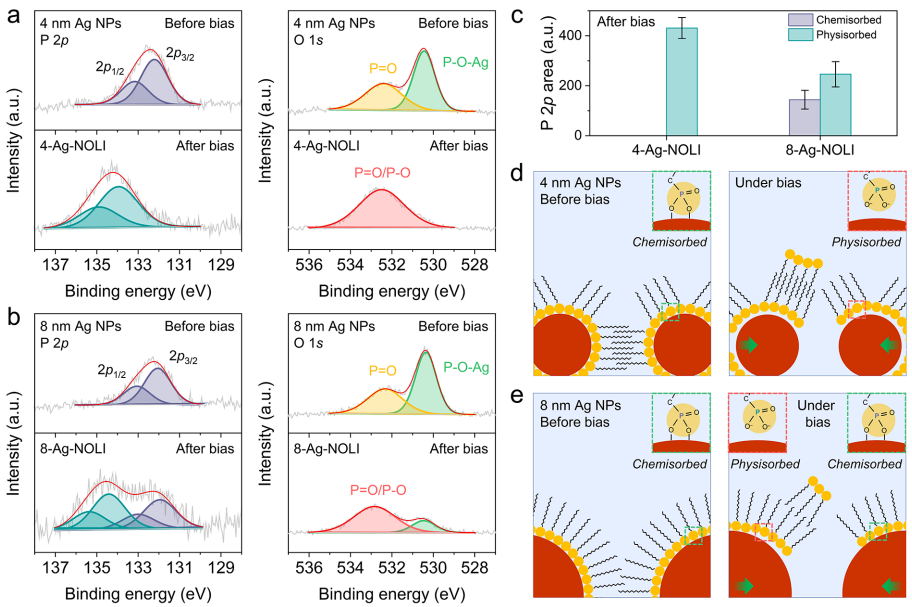

Figure 5. Formation of a ligand layer under bias from interdigitated ligands. a, **b**, X-ray photoelectron spectroscopy (XPS) P 2*p* and O 1*s* spectra of the assembled 4 nm (**a**) and 8 nm (**b**) Ag NPs, and the resultant 4-Ag-NOLI (**a**) and 8-Ag-NOLI (**b**) after 2 min of bias at –0.68 V vs. RHE. P 2*p* peaks were deconvoluted into $2p_{1/2}$ and $2p_{3/2}$. Purple in the P 2*p* XPS spectra represents the chemisorbed state of ligands, while cyan represents the physisorbed state. Likewise, green (P-O-Ag) in the O 1*s* XPS spectra indicate the chemisorbed ligand state, while pink (P=O/P-O) represents the physisorbed state. **c**, P 2*p* peak area integrated after bias for 2 min. The peaks representing chemisorbed and physisorbed ligand states were separately integrated. **d**, **e**, Schematics illustrating the behavior of interdigitated ligands under bias for the assembled 4 nm (**d**) and 8 nm (**e**) Ag NPs. Insets show the binding states of ligands before and under bias for each case. Green arrows indicate the motion of Ag NPs under bias resulting in NP fusion. Only two particles are shown for clarity in each case.

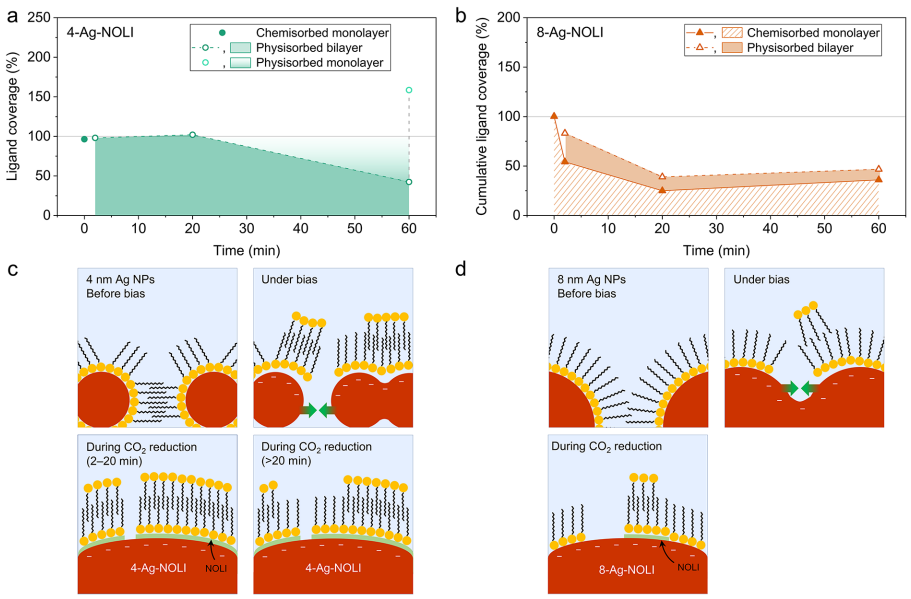

Figure 6. Ligand layer coverage and suggested ligand structure for Ag-NOLI catalysts. a, **b**, Ligand layer coverage of 4-Ag-NOLI (**a**) and cumulative ligand coverage of 8-Ag-NOLI (**b**) during CO_2 electrocatalysis estimated from XPS analysis. In **a**, green shaded area indicates the ligand layer coverage when physisorbed bilayer configuration is assumed. The dashed gray vertical line indicates the ligand layer coverage with two boundary conditions. Lower and upper bounds are complete bilayer and monolayer configurations, respectively. Cyan shaded area with gradient indicates potential coverage of physisorbed monolayer. In **b**, brown shaded area indicates the ligand layer coverage when physisorbed bilayer configuration is assumed. The hatched area represents chemisorbed ligand coverage. **c**, **d**, Schematics illustrating the overall process of a structurally ordered ligand layer formation for 4-Ag-NOLI (**c**) and 8-Ag-NOLI (**d**) under bias, and their suggested ligand layer structures during CO_2 electrolysis.

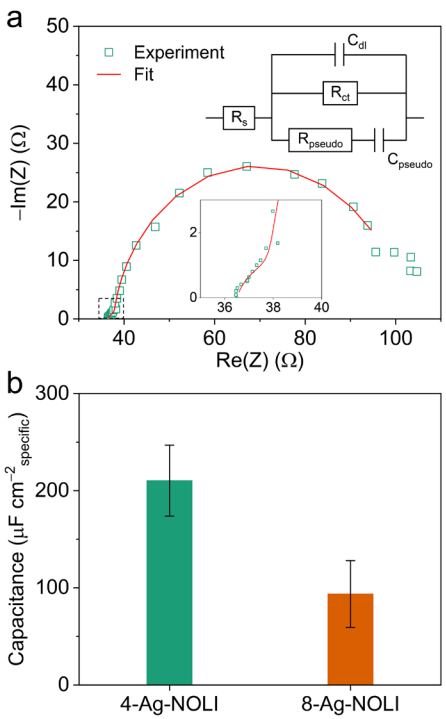

Figure 7. Pseudocapacitive characteristics and specific capacitance comparison of the NOLI for Ag-NOLI catalysts. a, Representative Nyquist plot of 4-Ag-NOLI obtained at –0.68 V vs. RHE. Insets show the equivalent circuit diagram used to fit the impedance data (top), and a high frequency region of the Nyquist plot (bottom). The equivalent circuit is composed of solution resistance (R_s), double layer capacitance (C_{dl}), charge transfer resistance (R_{ct}), pseudocapacitance (C_{pseudo}), and charger transfer resistance for pseudocapacitance (R_{pseudo}). **b**, Specific capacitance measured for the Ag-NOLI catalysts.

For Table of Contents Only